Article

Three-Dimensional Structure of the Intercalated Disc Reveals Plicate Domain and Gap Junction Remodeling in Heart Failure

Christian Pinali,[1] Hayley J. Bennett,[1] J. Bernard Davenport,[1] Jessica L. Caldwell,[1] Tobias Starborg,[2] Andrew W. Trafford,[1] and Ashraf Kitmitto[1,*]

[1]Institute of Cardiovascular Sciences, Faculty of Medical and Human Sciences and [2]Faculty of Life Sciences, University of Manchester, Manchester, United Kingdom

ABSTRACT   The intercalated disc (ICD) orchestrates electrochemical and mechanical communication between neighboring cardiac myocytes, properties that are perturbed in heart failure (HF). Although structural data from transmission electron microscopy two-dimensional images have provided valuable insights into the domains forming the ICD, there are currently no three-dimensional (3D) reconstructions for an entire ICD in healthy or diseased hearts. Here, we aimed to understand the link between changes in protein expression in an ovine tachypacing-induced HF model and ultrastructural remodeling of the ICD by determining the 3D intercalated disc architecture using serial block face scanning electron microscopy. In the failing myocardium there is no change to the number of ICDs within the left ventricle, but there is an almost doubling of the number of discs with a surface area of $<1.0 \times 10^8$ μm^2 in comparison to control. The 3D reconstructions further revealed that there is remodeling of the plicate domains and gap junctions with vacuole formation around and between the contributing membranes that form the ICDs in HF. Biochemical analysis revealed upregulation of proteins involved in stabilizing the adhesive and mechanical properties consistent with the morphological changes. Our studies here have shown that in tachypacing-induced HF mechanical stresses are associated with both structural and molecular alterations. To our knowledge, these data together provide novel, to our knowledge, insights as to how remodeling at the molecular and structural levels leads to impaired intercellular communication.

INTRODUCTION

The synchronous spread of the force of contraction through the myocardium is facilitated by intercalated discs (ICDs), structures that provide cell-to-cell mechanical connections and mediate electrochemical communication (1). The ICD is formed by a specialized region of the sarcolemma between the ends of each abutted cell. Two-dimensional (2D) transmission electron microscopy (TEM) of tissue sections has contributed greatly to our understanding of ICD morphology showing how ICDs are formed by an interdigitation of the sarcolemma with a crisscross topology between the myocytes in a direction orthogonal to the long axis of the myofilaments (1,2). The ICD has an undulating structure and thin filaments from the sarcomere connect to bundles of folded membrane commonly referred to as plicate domains. There are typically several distinct plicate domains within an ICD that are connected by longitudinal segments, interplicate domains, also referred to as the nexus. ICDs are composed of three functional types of cell junctions; desmosomes (or macula adherens) that act to adhere the opposing cell membranes providing mechanical stability through binding to intermediate filaments (3,4); adherens junctions endowing mechanical strength across the myocar-

dium by anchoring actin (5); gap junctions that are fundamental for the transmission of electrical and chemical stimuli between cells and facilitate the spread of the action potential (6,7). There are also regions, termed the area composita where both the adherens junctions and desmosomes co-localize (8). In addition, the regions where the myofibrils meet the apices of the plicae and area composita are collectively referred to as transitional junctions (9,10).

More than two hundred proteins are associated with the ICD (11). Of these proteins connexin43 (Cx43) has been identified as the principal component of gap junctions in ventricular myocytes, with connexin40 and connexin45 also contributing, but to a lesser extent, to the electrophysiological properties of the cardiac myocytes (12). The connexins provide a low resistance portal for the transmission of electrical impulses and chemicals between cells. N-cadherins (N-Cad) form complexes with the α-, β-, and γ-catenin proteins at the adherens junctions and facilitate calcium-dependent cell adhesion between adjacent cardiac myocytes and attachment sites for myofibrils (5).

Single point mutations and changes to ICD protein expression patterns and localization are linked to a number of cardiovascular disorders in a range of animal models and patients (13). For example, arrhythmogenic right ventricular cardiomyopathy is associated with mutations in proteins of the desmosomes (14), morphological changes to the

organization of the plicate domains (15), and a loss of Cx43 (16). A change to Cx43 abundance, mainly downregulation and redistribution, has also been reported in heart failure (HF) models (17–19). However, current data regarding alterations to ICD protein composition in HF is inconsistent. For example, in a model of compensated hypertrophy an upregulation of Cx43 was reported (20), although another study employing a rabbit pressure-volume overload model found Cx43 levels were reduced but with no change to N-Cad and β-catenin expression (21). In contrast, N-Cad levels have been reported to increase, with a reduction and redistribution of Cx43 in the left ventricle, in a canine model of HF induced by rapid pacing of the right ventricle (22).

Currently, there are no high-resolution three-dimensional (3D) data for entire ICDs within the myocardium. The only 3D data available have come from the application of scanning electron microscopy (SEM) techniques. However, SEM affords much lower resolutions than TEM and images only one surface of the intercalated disc (23,24). We have recently reported the application of serial block face scanning electron microscopy (SBF-SEM) for the reconstruction of cardiac myocytes (25). We determined the architecture of the cardiac t-tubule system, invaginations of the sarcolemma, and showed remodeling of the tubules together with the sarcoplasmic reticulum in an ovine model of HF. Given that the ICD represents another specialized region of the sarcolemma, we investigated the structure of ICDs within the left ventricle and determined 1) whether they undergo remodeling in an ovine tachypacing-induced HF model and 2), whether expression levels of ICD junction proteins Cx43 and N-Cad, and associated proteins, that influence the electromechanical properties of the myocardium, are modified in parallel. We have employed SBF-SEM to generate, to our knowledge, the first high-resolution 3D structure of ICDs from control and failing cells within the left ventricle, revealing remodeling of the plicate and nexus domains leading to a change in the gap junction environment. Furthermore, biochemical analyses found upregulation of N-Cad/catenin complexes forming the adherens junctions, together with an increase in desmin levels, a constituent of desmosomes, and the gap junction protein Cx43. We describe here how in response to mechanical pacing the cardiac myocytes remodel at both a molecular and cellular level.

MATERIALS AND METHODS

Tachypacing-induced HF

Welsh ewes, aged 18 months were employed for this study. HF was induced by right ventricular tachypacing as described previously (26,27) ($n = 4$). Sheep were intubated and ventilated (15 breaths/min) and anesthesia was induced and maintained with isoflurane (1–4% v/v in oxygen). The analgesia meloxicam (0.5 mg kg^{-1}) and antibiosis enrofloxacin (2.5 mg kg^{-1}) were administered subcutaneously. All procedures were carried out in accordance with the United Kingdom Animals Act (Scientific

Procedures) of 1986 and the University of Manchester's ethical review process. Upon presentation of clinical symptoms of HF the sheep were killed with an overdose of pentobarbitone (200 mg/kg i.v.). Hearts were perfused with calcium free Tyrode's solution and 1–2 mm^3 cubes of left ventricle were immediately excised from control and HF hearts and prepared for electron microscopy studies as previously described (25). Multiple blocks were prepared for each myocardium and those showing good contrast and sample preservation were selected for SBF-SEM analysis.

Image analysis and 3D reconstruction of intercalated discs

An FEI Quanta 250 FEG SEM equipped with a Gatan 3View ultramicrotome was used to collect a sequence of images generated by imaging the block face after every cut. An operating voltage of 3.8 kV and vacuum setting of 0.5 torr were employed. To obtain data for the organization of the ICDs within the left ventricle, we collected data sets at low magnification (×850) with a cut depth of 150 nm for voxel sizes (X, Y, Z) 45, 45, 150 nm per pixel. Higher resolution images for 3D reconstructions were acquired at ×2500 magnification and cutting depth of 50 nm generating data at 15, 15, 50 nm (X, Y, Z) at the pixel level. The ICDs were segmented either in Fiji (28) or IMOD (29) and visualized using Chimera (30). In IMOD, the 3D disc structures were orientated to present the plicae in a vertical orientation to demark the tips of the folds and connect these points to form a surface connecting all the peaks (upper surface) and the troughs (lower surface) in 3D. The distance between the upper and lower surfaces gives the effective thickness of the plicate domain. Quantification of the longitudinal domains of the interplicate (nexus) segments and the gap junctions around and near the plicae were also undertaken using IMOD. Domains composed of only plicae were individually segmented for surface area measurements. Gap junctions localized to the plicae domains were also segmented and the surface areas calculated. The electron dense plaques (desmosomes and adherens junctions) were often less well resolved through the serial images compared to the gap junctions, which were very distinct, therefore plaque surface area measurements could not be confidently measured and so only the number of plaques was analyzed. Random segments of 10 μm across the various ICDs in each group were assessed for the presence of the plaques. The distance of 10 μm was selected based upon observations that within this region there were multiple electron dense plaques. All features were measured in multiple cells from each animal per experimental group.

Protein isolation and quantification

Tissue samples were homogenized in the presence of RIPA buffer containing protease inhibitors. Protein levels in the lysates were analyzed using SDS-PAGE (stain-free gels, Bio-Rad) and Western blotting (BioRad Trans-Blot Turbo transfer apparatus and PVDF MICDi transfer packs). Protein expression level changes were determined using the technique of total protein using stain-free gels (31), because the housekeeping proteins GAPDH and β-actin have been found to change in this model of HF (26). Transfer was verified using stain-free imaging (Fig. S1 in the Supporting Material). The blots were blocked with 5% milk in TBST, followed by incubation with primary and secondary antibodies for 1 h at room temperature, each followed by three 10 min washes in TBST at room temperature and incubation in Clarity Western ECL substrate chemiluminescent detection reagent (Bio-Rad) for 5 min before image acquisition. The chemiluminescent blots were imaged with the ChemiDoc MP system imager (Bio-Rad). Control and HF samples were run on the same gel for each antibody so that the exposure conditions were identical. The chemiluminescent signal intensity of a given protein was normalized to the relative quantification of the corresponding intensity of the total protein. Data from each replicate were normalized and then averaged across the replicates. Normalized data are plotted with standard error of the mean ($\pm$ SEM).

Statistical analysis

ICD structural features were analyzed from HF sheep ($n = 4$) and age-matched control sheep ($n = 4$). All data were analyzed using either a one-way analysis of variance or Student's t-test as appropriate using GraphPad Prism 6.0. Data are expressed as mean $\pm$ SEM unless otherwise stated. Data were considered significant when $P < 0.05$.

RESULTS

Intercalated disc organization within the sheep left ventricle

Using SBF-SEM at a low magnification ($\times 850$) we have imaged the ICDs formed between cardiac myocytes within the left ventricle. Fig. 1 shows the characteristic staircase-like organization of the ICDs forming both up and down risers within the same disc. Segmentation of each disc revealed that the shape and size of the discs is variable (Fig. 1, C and D), with surface areas ranging from $5.86 \times 10^6 \ \mu m^2$ to $1.11 \times 10^9 \ \mu m^2$ (see Fig. S2); 54 discs analyzed, $n = 4$.

3D reconstruction of the ovine intercalated disc

Employing higher magnifications, ($\times 2500$) revealed details of the domains forming the ICD as shown in Fig. 2 (also see Movie S1). A comparison of the ICD morphology with that derived from early TEM of thin sections (1,4) shows that structural features are consistent. In the SBF-SEM images, we are viewing the stain that accumulates between the membranes from each contributing cardiac

myocyte. The undulating plicate folds are clearly resolved (Fig. 2 A) as are the gap junctions, where the intermembrane distance is narrowed (Fig. 2 B). Electron dense plaques (desmosomes and adherens junctions) were also identified as shown in Fig. 2 C. To our knowledge, we have determined the first 3D structure for ICDs formed between neighboring myocytes in situ within the sheep left ventricle from these types of data as shown in Fig. 3. Both surfaces of the ICD are shown in Fig. 3 as they extend into the adjacent cardiac myocytes. The plicae only previously imaged as folds in 2D are now seen to form finger-like protrusions. Furthermore, a cross section through the disc also reveals how the plicae form terraces separated by a vertical wall, the nexus (or interplicate domain), which is exposed to the cell interior on either side.

Many studies have assumed that the amplitude of the folds seen in the 2D TEM images corresponds to the height of the projections, which depending upon the angle of tissue sectioning may be correct in some instances. We have tracked two plicate folds (*segmented in yellow and green*), which are separated by an interplicate domain (*blue*) through the 3D volume, as shown in Fig. 4 A, and found that the plicate contours correspond in these images to an oblique cross section, which stack on top of each other to form the finger-like protrusions, as shown in Fig. 4 B, and therefore the amplitude (trough to peak distance) does not correspond to the length of the projection in 2D or how far it extends into the cardiac myocyte. 3D reconstructions are necessary to determine the distance between the tips and troughs of the individual protrusions (Fig. 4 C). Here, we found an average plicate amplitude of 803 ± 20 nm
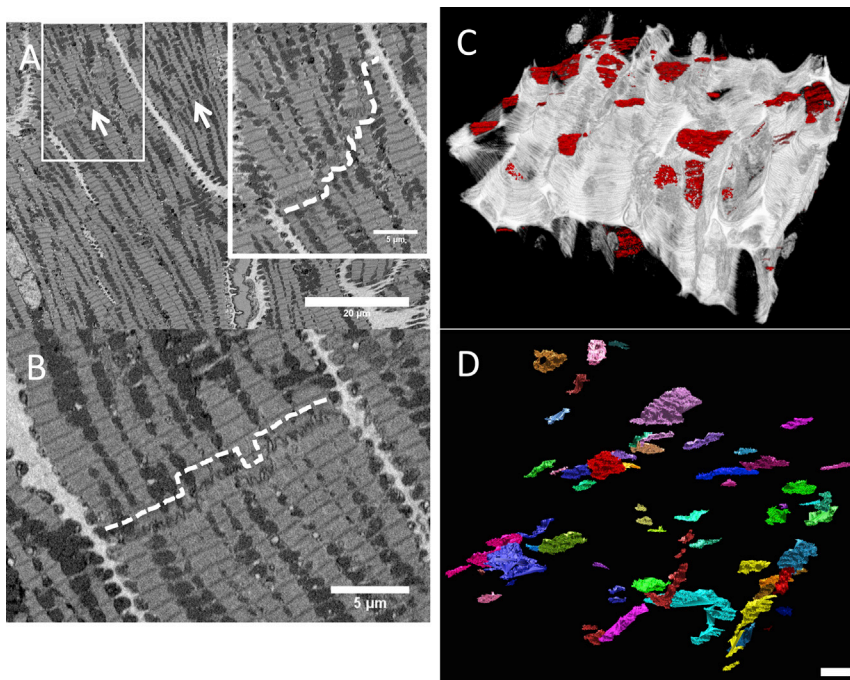

FIGURE 1 ICDs vary in width according to the cross-sectional position within the cell. (A) Portion of a serial block face image at $\times 850$ magnification from control sheep left ventricle. Arrows indicate the ICDs formed between the ends of adjacent cardiac myocytes. Inset: magnified area of the region within the box showing the staircase-like arrangement of an ICD (*dashed white line*). (B) The pattern of steps can both be up and down and changes within a single disc through the cell volume (*dashed white line*). (C) Reconstruction of the extracellular matrix (*white*) and the ICDs (*red*) Height of reconstruction = 375 μm. (D) 3D reconstruction of the ICDs (*assorted colors*) illustrating the variation in the shape and size (Scale bar = 20 μm). To see this figure in color, go online.
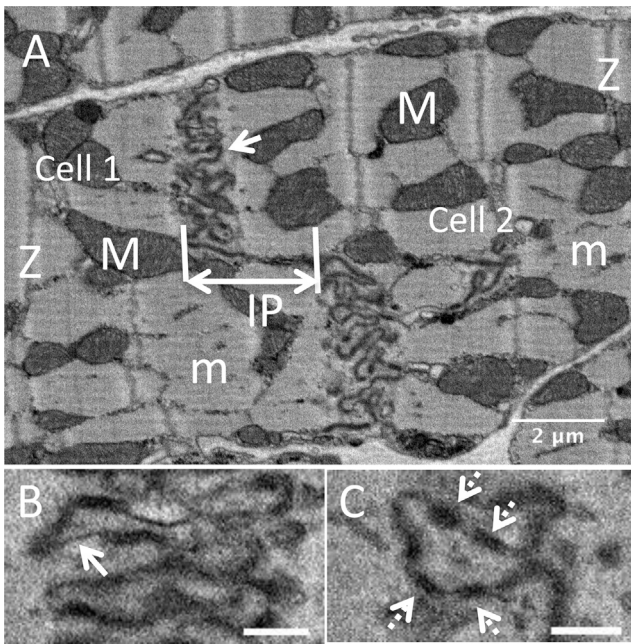
FIGURE 2 Serial block face images of an intercalated disc (*control*) taken at ×2500 magnification. (*A*) ICD exhibiting the characteristic winding morphology, arrow highlights plicae; IP, linear interplicate domain (*nexus*); m, myofilaments; M, mitochondria; Z, Z-line. (*B*) Gap junctions (*white arrows*) are where the intermembrane distance is restricted so there is less stain accumulation. (*C*) Electron dense plaques (*dashed-white arrows*). Scale bar = 500 nm.

with a mean base diameter of 271 ± 19 nm for each finger-like projection (Fig. 4 *D*). Segmentation of the interplicate (nexus) regions through the 3D volumes also determined the average length to be 2304 ± 353 nm.

The intercalated disc undergoes remodeling in HF

Analysis of the number of ICDs in control and failing ventricle found no significant difference; 17.0 ± 1.5 control and 19.8 ± 1.7 HF (within $1 \times 10^5 \mu m^3$ tissue; $n = 4$). The surface area of the HF discs also exhibited a wide spread, as seen in control, ranging from $3.43 \times 10^6 \mu m^2$ to $1.6 \times 10^9 \mu m^2$ (49 discs analyzed). However, a frequency analysis showed that in HF ventricles 41% of ICDs had a surface area $<1.01 \times 10^8 \mu m^2$ compared to 22% of control ICDs (Supporting Material data and Fig. 2).

A 3D reconstruction of an exemplar HF ICD orientated to show the finger-like projections extending from one face is presented in Fig. 5, *A* and *B*. Measurement in 3D of the plicate domains from HF ICDs found that they typically span at least one sarcomere with a mean height of 2255 ± 305 nm ($P < 0.01$) and thus are ~3× more extended compared to control (803 ± 20 nm), as shown in Fig. 5, *C* and *D*. The fold heights of HF ICDs also showed less consistency with a coefficient of variation of 33.2% (compared to 6.0% for control plicae). Despite the approximate three-fold extension of the plicae amplitudes we determined
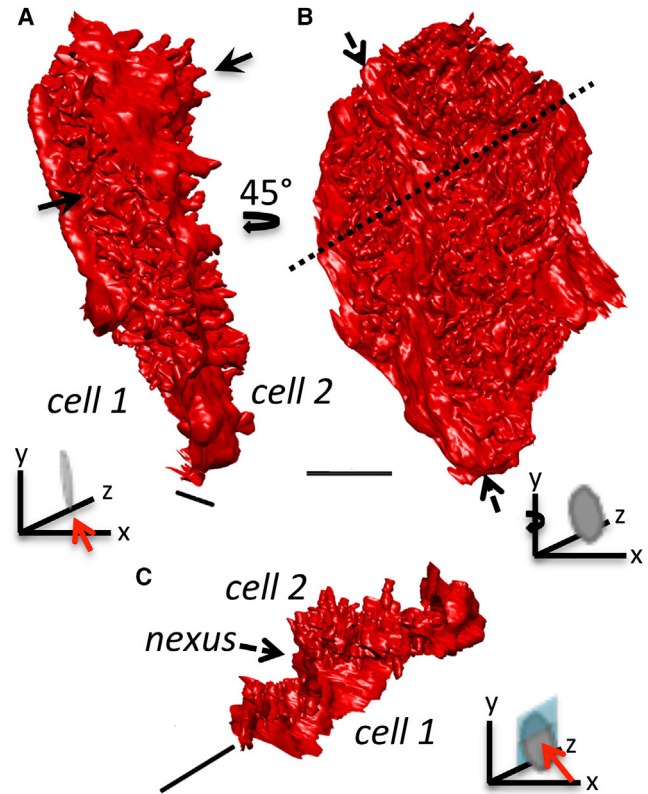

FIGURE 3 3D reconstruction of a control intercalated disc. (*A*) Projections (*plicae*) extend from both surfaces of the ICD (*black arrows*). (*B*) The ICD has an undulating surface projecting into the cardiac myocytes. The dashed arrows indicate a nexus domain that runs along the long axis of the disc. (*Dashed line* is the position of the clip plane used to generate the image in *C*.) (*C*) The interplicate (*nexus*) domain forms an almost vertical wall in this orientation and is exposed to both adjacent cardiac myocytes. Scale bar = 2 μm. Figure insets: direction of view (*red arrow*) indicators, the disc shape represents the ICD and position of the clipping plane is shown in cyan. To see this figure in color, go online.

that there was no change to the base width of individual projections, between the control and HF plicate projections with the average width of 266 ± 11 nm. We sampled portions of ICDs in both control and HF that contained only plicae and measured the ratio of the surface of the plicae with respect to the area from which they projected (footprint) finding roughly a doubling in HF compared to control (12.8 ± 2.3 (control) and 26.1 ± 3.5 (HF), $P = 0.0376$).

The interplicate regions (nexi) were also significantly more extended than in control ICDs with a height of 5648 ± 540 nm ($P < 0.001$), Fig. 5 *E*. However, they were found to be less exposed compared to control, due to the surrounding elongated plicae. In addition to gap junctions forming the nexi, we also identified gap junctions clustered around the plicae in both control and HF ICDs. We found no change to the dimensions of this pool of gap junctions with mean lengths of 421 ± 34 nm (control) and 438 ± 35 nm (HF) and surface areas of
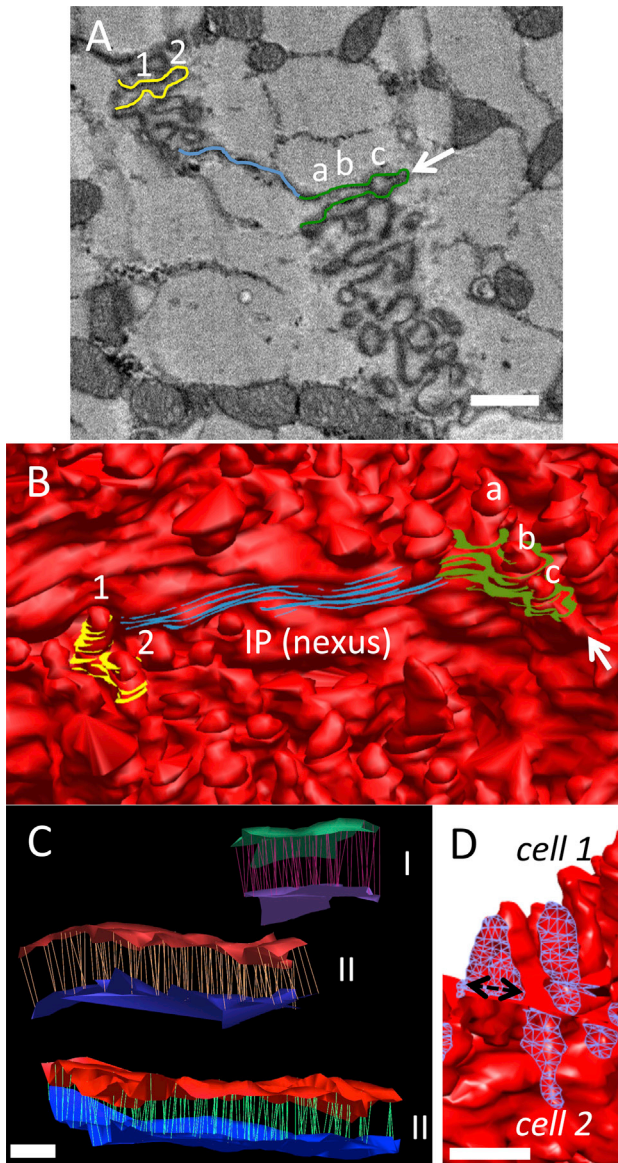
FIGURE 4   3D reconstructions from SBF-SEM volumetric data reveals plicae morphology (A) Serial block face image showing a portion of an ICD with two folds contoured in yellow and green, and the nexus in blue. The arrow indicates the tip of the green fold. Scale bar = 500 nm. (B) Corresponding portion of the 3D ICD volume illustrates how the fold segmented in yellow does not correspond to the height/amplitude of the finger-like projection but to an oblique cross section and contributes to two projections (labelled 1 and 2). Similarly, the single green fold in (A) contributes toward three individual finger-projections in 3D (labeled a, b, and c). (C) Measurement of the height (amplitude) of the plicae by connecting the tips and the troughs of the finger-like projections to define the surface topology (between 50 and 500 individual measurements made per plicate domain) three plicate domains within a single ICD are shown. Plicate I; upper and lower surfaces are colored green and purple, plicate II; red and dark blue, plicate III; red and light blue. The lines between the two sheets indicate the individual height measurements taken in 3D. Scale bar = 500 nm. (D) The base diameter of the finger-like projections (indicated by the double-headed arrow) was also measured (1123 individual folds analyzed). A section of the ICD has been clipped and the surface capped with a blue mesh to illustrate this dimension. Scale bar = 500 nm. To see this figure in color, go online.

77676 ± 5560 nm^2 and 90967 ± 3885 nm^2, respectively (82 and 104 gap junctions measured for control and HF). Additional analysis of those regions of discs formed by plicae (e.g., as shown in Fig. 7 D) revealed that gap junctions covered $2.3\% \pm 0.6\%$ of the plicae surface area in control whereas in HF the coverage was $0.4 \pm 0.1\%$ ($P = 0.0807$). Moreover, the number of gap junctions within domains formed only by plicae (normalized to a plicae surface area of 20 μm^2) within HF ICDs was significantly less (1.3 ± 0.4) compared to control (8.3 ± 1.0); $P = 0.0106$. Furthermore, 3D reconstruction of the gap junctions at the plicae in both control and HF ICDs revealed that in control ICDs they are exposed across the surface of the disc as shown in Fig. 6, whereas in the failing tissue they are less exposed and buried within the ICD organization due to the distension of the plicae (also see Movies S2 and S3). The electron dense plaques (desmosomes and adherens junctions), which decorate the plicate folds, (Fig. 2 C), were determined to be shorter in HF, 130 ± 5 nm (73 plaques measured) compared to control 173 ± 6 nm (70 plaques measured; $P < 0.001$) but a trend toward an increase in plaque number was observed in HF; 4.0 ± 0.4 compared to 5.1 ± 0.4 (per 10 μm segments of ICD) $P = 0.06$.

HF ICDs are characterized by surface vacuoles

Our study further identified that a large number of vacuoles were present within ICDs between failing cells, as shown in Fig. 7. We noted that the vacuoles were only found at the ICD and that there was good preservation of the surrounding cardiac myocyte ultrastructure, indicating that it was unlikely they had formed due to poor sample preparation techniques. The vacuoles could be grouped into two types based upon location with respect to the ICD; intercellular (extracellular), formed between the cardiac myocytes, with minimum and maximum diameters of $107 \pm 4 \times 189 \pm 6$ nm, and intracellular, cytosolic vacuoles measuring 243 ± 14 and 406 ± 25 nm juxtaposed to both sides of the ICDs. The percentage of the surface area of the vacuoles relative to the surface area of the ICD was $1.4 \pm 0.8\%$.

There were much fewer of the cytosolic vacuoles compared to the intercellular type. Examination of control ICDs did not find any of the intracellular vacuoles and only an occasional intercellular vacuole present within the extracellular space (Supporting Material data and Fig. 3); this was found to be the case for all of the control ICDs examined in this study. Reconstruction of the individual vacuoles (Fig. 7, B and C) showed that the vacuoles are extensive and distributed across the entire disc in HF. Furthermore, examination of the vacuole distribution around the plicae revealed that they were often buried between folds and were also found at the tips of the plicae (Fig. 7 D). We next considered whether the intercellular vacuoles could be correlated to changes in the distribution of
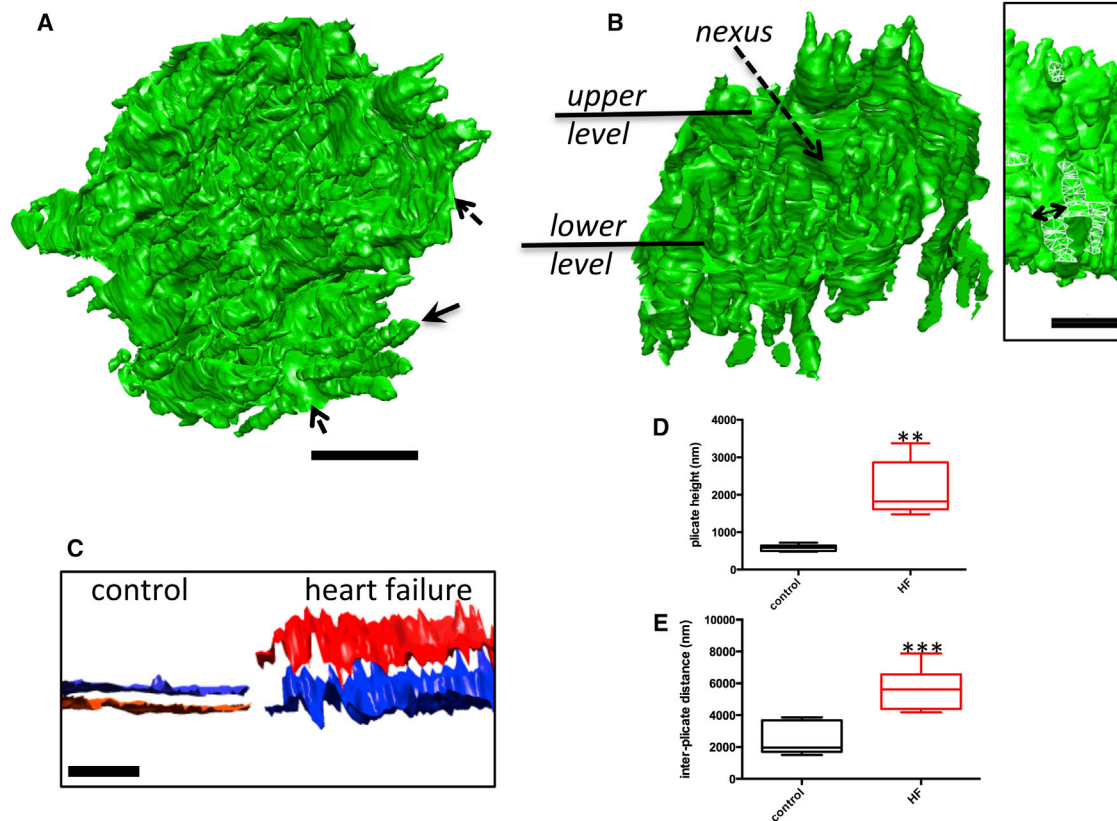
FIGURE 5 3D reconstruction of ICDs from failing cells reveals elongated plicae. (*A*) Plicae (*indicated by arrows*) are extended compared to control, dashed arrow indicates interplicate region. (*B*) Removal of a portion of the ICD reveals that interplicate domains also separate the distended projections. Scale bar = 2 μm. Inset, double-headed arrow indicates base diameter of the finger-like projections; surface capped with a white mesh for clarity. Scale bar = 2 μm. (*C*) The height of the ICD plicae has increased in the failing myocardium, indicated by the separation between the two surfaces delineating the plicate peaks and troughs. Scale bar = 5 μm (1320 plicae analyzed, 6 ICDs). (*D*) Box and whiskers plot shows increased plicae heights for HF ICDs ($P < 0.01$). The dividing line is the median and the upper and lower bars the maximum and minimum values. (*E*) Plot showing that the length of the inter-plicate domains (nexus) increases in HF ICDs ($P < 0.001$). To see this figure in color, go online.

the gap junction protein Cx43. Employing immunolabeling techniques and confocal microscopy the distribution of Cx43 was analyzed, finding that in the healthy ventricular tissue it is highly localized to the intercalated discs (Fig. S4 *A*). However, no change to the protein cellular distribution was observed for sections from the HF ventricle (Fig. S4 *B*).

From our data we also observed that mitochondria are often tethered to the tips of plicae or are juxtaposed to gap junction nexi as shown in Fig. 8, *A* and *B*; a spatial relationship previously reported (32). The 3D reconstructions of mitochondria adjacent to the ICD reveals how the gap junctions encase the mitochondria as shown in Fig. 8, *C* and *D*. Mitochondria near to the ICDs in both healthy and failing cardiac myocytes were measured and the diameters (along and orthogonal to the myofilaments) were determined to be 1196 ± 78 × 697 ± 141 nm and 1064 ± 48 × 810 ± 87 nm, respectively (mitochondria measured; 1378 control and 818 HF), finding a trend toward enlargement of the mitochondrial diameters orthogonal to the myofilaments in HF myocytes ($P = 0.0505$).

Proteins associated with ICD specialized domains are upregulated in HF

Given the morphological changes to the ICD architecture in HF, we next investigated whether remodeling was paralleled by changes to protein expression. Fig. 9 shows the changes to the expression profiles of proteins associated with the ICD electrochemical and mechanical properties (for blots see Fig. S6). Proteins associated with the desmosomes, desmin and γ-catenin (plakoglobin) were upregulated as was the N-Cad/catenin macromolecular complex at the adherens junctions. The gap junction protein Cx43 and cytoskeletal protein spectrin were also found to be more abundant, whereas expression levels of vinculin and α-actinin remained unchanged.

DISCUSSION

The principal findings from this study are that in an ovine tachypacing-induced HF model there is remodeling of the intercalated disc; in particular, the plicate domains
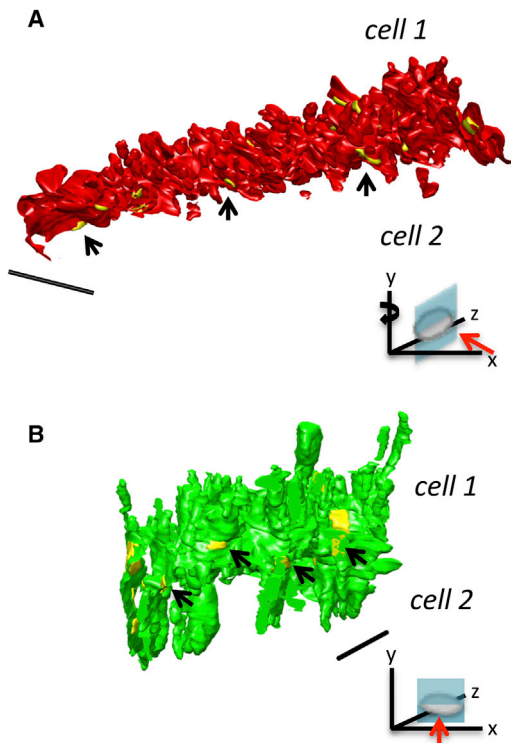
FIGURE 6 The gap junctions associated with the plicate domains are buried between the elongated projections formed in HF. (A) Removal of a portion of the control ICD shows how the gap junctions are exposed and nestled at the base of the plicae. (B) The gap junctions in HF ICDs are sandwiched between the elongated projections so that they are located deep within the ICD structure. Scale bar = 5 μm. Figure inset; direction of view indicator (red arrow), the disc shape represents the ICD and position of the clipping plane is shown in cyan. To see this figure in color, go online.

and interplicate regions, accompanied by an upregulation of Cx43 and proteins forming adherens junctions and desmosomes.

Structural and molecular modifications to the ICDs in HF

A novel finding, to our knowledge, from this study is that there is an increase in the number of ICDs with surface areas $<1.01 \times 10^8 \ \mu m^2$. A higher number of smaller ICDs may be linked to reports of increased intercellular resistivity and conductance anisotropy in HF models (33). A further consequence of tachypacing-induced HF is an extension of the plicae and a doubling of the surface area. Therefore, despite an increase in the frequency of ICDs with a smaller surface area, the plicae are enlarged, which will act to provide local areas with increased contact surfaces between the two cells. An increase in plicae amplitude has also been recently described as part of the mechanism that promotes myocyte lengthening during development (34) with the scaffold protein N-RAP shown to be instrumental for myofibril assembly (35) and in the adult cardiac myocyte N-RAP is
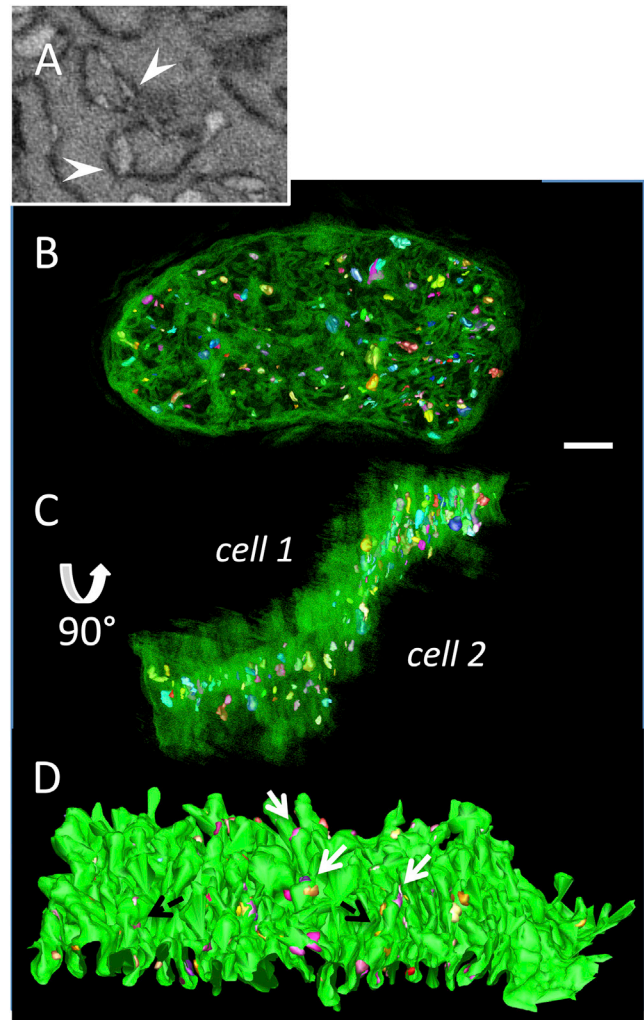

FIGURE 7 Vacuoles decorate HF ICDs (A) Serial image of a portion of a HF ICD showing details of intercellular vacuoles sandwiched between the two membrane leaflets (arrowheads); box size 2.0 × 1.4 μm. (B) 3D reconstruction of a HF ICD (green) and the associated vacuoles (segmented in range of colors). (C) ICD after rotation around the x axis showing that the vacuoles have formed over both sides of the disc and are not concentrated to any particular region. Scale bar = 2 μm. (D) 3D reconstruction of a plicate domain and intercellular vacuoles. White arrows indicate vacuoles forming at the tip of the plicae and black arrows the vacuoles between the plicae. Length of reconstruction = 10.43 μm. To see this figure in color, go online.

exclusively localized to the ICD (36). Here, we found that N-RAP was upregulated in HF. Reactivation of the fetal gene program has been described as a pathological response to hypertrophy and HF (37). Consequently, the changes to protein expression patterns and associated structural remodeling described here may in part reflect a reversion to fetal ICD protein expression and explain why the adaptation of the plicate domains is a feature of a range of cardiovascular disease phenotypes. A result of plicae remodeling is a change to the local environment of the associated gap junctions. In the healthy myocyte the gap junctions are exposed
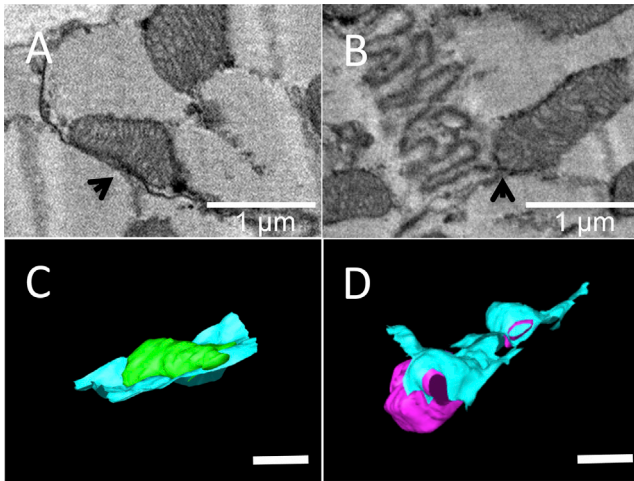
FIGURE 8 Mitochondria are in contact, or tethered, to ICDs. Portions of serial block face SEM images for control ICDs showing examples where a mitochondrion is (*A*) in contact with a gap junction in the interplicate region (*arrow*) and (*B*) tethered to the tip of a plicate fold (*arrow*). (*C* and *D*) 3D reconstruction of the mitochondrion and ICD showing in (*C*) how the ICD forms a basket shape in which the mitochondrion (*green*) sits in and (*D*) where the ICD wraps around one end of a mitochondrion (*magenta*). Scale bar = 1 μm. To see this figure in color, go online.

to the surrounding milieu, whereas in HF they are buried. Therefore, this structural reorganization may alter filtering and diffusion properties of the gap junction protein Cx43 not only between adjacent myocytes but also within the cytosol. Equally, the resultant change to the intracellular environment near to the gap junctions may foster pathological stimuli.

A loss of desmin is considered a hallmark of arrhythmogenic right ventricular cardiomyopathy (14) yet in this study we found that desmin is 4–5 times more abundant in HF compared to control. However, our data are in agreement
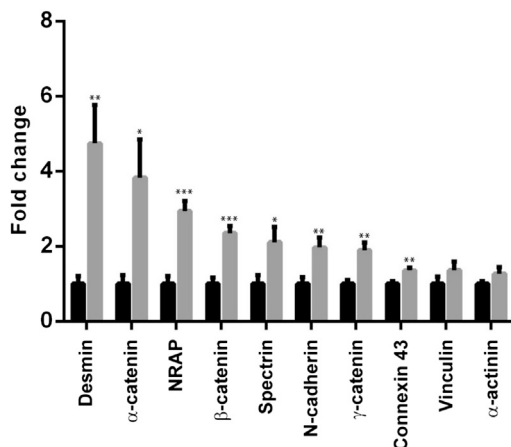

FIGURE 9 Remodeling of the ICD at the molecular level in HF. Histogram summarizing the data for each blot with the matching control (*n* = 7; three technical replicates). Black bars are normalized controls, gray bars are HF expression levels.

with a previous study of a canine tachypacing model of dyssynchronous HF, reporting elevated levels of desmin, which was also shown to form cardiotoxic amyloid-like oligomers (38). Although we did not observe any cytoplasmic densities in our images that could correspond to desmin polymers, desmin overexpression has been suggested to be a compensatory response in hypertrophy (39) and HF (40). We did not find any change to levels of vinculin, another cytoskeletal protein. In a model of pressure overload hypertrophy vinculin has been reported to be downregulated (40), whereas in the human failing heart it has been shown to be overexpressed (41). However, the increase in abundance of N-cadherin and α-, β-, and γ-catenin and spectrin is consistent with junction remodeling to consolidate the adhesion properties of the ICD in response to increased ventricular mechanical load. Furthermore, although the electron dense plaques decorating the fold projections were found to be shorter in HF, there was a trend toward an increased number of plaques. However, a limitation of this method for calculating the number of plaques lies with it not being possible to exactly match the same number of plicae within the regions examined (as discussed in the Materials and Methods).

The formation of vacuoles in HF will affect cell-to-cell communication

As yet, we do not understand the mechanisms underlying intercellular vacuole formation but from a structural perspective they appear to be distinct from vesicular activity or annular gap junctions (42,43). Gap junctions are considered the weakest link within the ICDs and have been reported to be lost after myocardial infarction (44). Conditional cardiac gene ablation of Cx43 has found that although there is no change to ICD architecture (45) the electrical properties of the heart are disturbed leading to fatal arrhythmias (46). Therefore, putative deformation of gap junctions associated with the plicae to form vacuoles will have the potential to lead to pockets of ventricular electrical dyssynchrony. Here, we showed for the first time, to our knowledge, that in the tachypacing-induced HF myocardium there is a reduction in the number of gap junctions distributed around the plicae and that this phenomenon cannot be explained by a redistribution of Cx43 within the cardiac myocyte. Intercellular vacuoles were found sandwiched between plicae (i.e., where gap junctions are often found) as well at the tips of the folds. Therefore, the data point toward gap junction remodeling as contributing toward intercellular vacuole formation, although there may also be other confounding factors and mechanisms involved. However, a consequence of vacuole formation within the extracellular space will be to potentially reduce the surface area and contact points between cardiac myocytes and to possibly impair cell-to-cell communication. Because we have shown that the length of the interplicate regions

composed of gap junctions in HF ICDs is more than doubled then the overall increase in Cx43 levels, despite the loss of gap junctions at the plicae, would be consistent with this structural adaptation.

An association between mitochondria and gap junctions forming the nexus has been previously described (32), a relationship suggested to facilitate Ca^{2+} transfer between the extracellular space and the mitochondria. The novel data, to our knowledge, from SBF-SEM provides an explanation as to how portions of gap junctions encircle adjacent mitochondria providing multiple sites for ion exchange and thus how disruption of this spatial relationship would impact upon Ca^{2+} buffering around the disc environment. We suggest that the intracellular vacuoles may be the space left after mitochondrial rupture close to the disc, as we have previously described rearrangement of myofibrillar mitochondria in this experimental model of HF (25). Although the dimensions of the intracellular vacuoles formed in HF do not exactly match those of mitochondria it may be that upon the collapse of the mitochondria, surrounding densely packed organelles extend to partially fill the vacuum (Supporting Material data and Fig. 5).

In summary, the data here show that the failing heart attempts to compensate for the mechanical stress due to the tachypacing by increasing the surface area and size of the plicate folds and size of the connecting interplicate domains. The morphological adaptation and concurrent upregulation of desmosome and adherens junction proteins may work to reinforce against an increased mechanical load to maintain cell-to-cell adhesion and electrochemical communication. The increase in abundance of the proteins associated with the ICD junctions described here shows some similarity to myocytes exposed to pulsatile stretching (47) rather than for example pressure-volume overload models (21) and thus suggests a phenotype related to mechanical load. However, in general there is a common pattern emerging of ICD structural remodeling across a diverse number of myocardial diseases. It therefore may be appropriate to propose that the ultrastructure of the ICD, particularly the plicate size, could potentially be used to not only differentiate between control and cardiac disease phenotypes but also perhaps as an indication of disease progression. Together the molecular and ultrastructural changes to the ICD composition advance our understanding of how electrochemical and mechanical communication is disturbed between neighboring cardiac myocytes in HF and the remodeling that occurs to combat mechanical stress.

SUPPORTING MATERIAL

Supporting Materials and Methods, six figures, and three movies are available at http://www.biophysj.org/biophysj/supplemental/S0006-3495 (14)04687-6.

REFERENCES

1. Forbes, M. S., and N. Sperelakis. 1985. Intercalated discs of mammalian heart: a review of structure and function. *Tissue Cell.* 17:605–648.

2. Severs, N. J., A. M. Slade, …, V. W. Twist. 1985. Ultrastructure of the sarcolemma and intercalated disc in isolated rat myocytes. *Basic Res. Cardiol.* 80 (Suppl 2):35–40.

3. Grimley, P. M., and G. A. Edwards. 1960. The ultrastructure of cardiac desnosomes in the toad and their relationship to the intercalated disc. *J. Biophys. Biochem. Cytol.* 8:305–318.

4. Forbes, M. S., and N. Sperelakis. 1975. The "imaged-desmosome": a component of intercalated discs in embryonic guinea pig myocardium. *Anat. Rec.* 183:243–257.

5. Zuppinger, C., M. Eppenberger-Eberhardt, and H. M. Eppenberger. 2000. N-Cadherin: structure, function and importance in the formation of new intercalated disc-like cell contacts in cardiomyocytes. *Heart Fail. Rev.* 5:251–257.

6. Severs, N. J. 1990. The cardiac gap junction and intercalated disc. *Int. J. Cardiol.* 26:137–173.

7. Severs, N. J. 1989. Gap junction shape and orientation at the cardiac intercalated disk. *Circ. Res.* 65:1458–1462.

8. Franke, W. W., C. M. Borrmann, …, S. Pieperhoff. 2006. The area composita of adhering junctions connecting heart muscle cells of vertebrates. I. Molecular definition in intercalated disks of cardiomyocytes by immunoelectron microscopy of desmosomal proteins. *Eur. J. Cell Biol.* 85:69–82.

9. Bennett, P. M., A. M. Maggs, …, J. C. Pinder. 2006. The transitional junction: a new functional subcellular domain at the intercalated disc. *Mol. Biol. Cell.* 17:2091–2100.

10. Bennett, P. M. 2012. From myofibril to membrane; the transitional junction at the intercalated disc. *Front Biosci (Landmark Ed).* 17:1035–1050.

11. Estigoy, C. B., F. Pontén, …, C. G. dos Remedios. 2009. Intercalated discs: multiple proteins perform multiple functions in non-failing and failing human hearts. *Biophys. Revs.* 1:43–49.

12. Desplantez, T., E. Dupont, …, R. Weingart. 2007. Gap junction channels and cardiac impulse propagation. *J. Membr. Biol.* 218:13–28.

13. Glukhov, A. V., V. V. Fedorov, …, I. R. Efimov. 2012. Conduction remodeling in human end-stage nonischemic left ventricular cardiomyopathy. *Circulation.* 125:1835–1847.

14. Oxford, E. M., M. Everitt, …, M. Delmar. 2007. Molecular composition of the intercalated disc in a spontaneous canine animal model of arrhythmogenic right ventricular dysplasia/cardiomyopathy. *Heart Rhythm.* 4:1196–1205.

15. Basso, C., E. Czarnowska, …, A. Rampazzo. 2006. Ultrastructural evidence of intercalated disc remodelling in arrhythmogenic right ventricular cardiomyopathy: an electron microscopy investigation on endomyocardial biopsies. *Eur. Heart J.* 27:1847–1854.

16. Saffitz, J. E. 2009. Arrhythmogenic cardiomyopathy and abnormalities of cell-to-cell coupling. *Heart Rhythm.* 6 (8, Suppl):S62–S65.

17. Peters, N. S., C. R. Green, …, N. J. Severs. 1993. Reduced content of connexin43 gap junctions in ventricular myocardium from hypertrophied and ischemic human hearts. *Circulation.* 88:864–875.

18. Severs, N. J., A. F. Bruce, …, S. Rothery. 2008. Remodelling of gap junctions and connexin expression in diseased myocardium. *Cardiovasc. Res.* 80:9–19.

19. Saffitz, J. E., and A. G. Kléber. 2004. Effects of mechanical forces and mediators of hypertrophy on remodeling of gap junctions in the heart. *Circ. Res.* 94:585–591.

20. Kostin, S., S. Dammer, …, J. Schaper. 2004. Connexin 43 expression and distribution in compensated and decompensated cardiac hypertrophy in patients with aortic stenosis. *Cardiovasc. Res.* 62:426–436.

21. Wiegerinck, R. F., T. A. B. van Veen, …, R. Coronel. 2008. Transmural dispersion of refractoriness and conduction velocity is associated with heterogeneously reduced connexin43 in a rabbit model of heart failure. *Heart Rhythm.* 5:1178–1185.

22. Akar, F. G., D. D. Spragg, …, G. F. Tomaselli. 2004. Mechanisms underlying conduction slowing and arrhythmogenesis in nonischemic dilated cardiomyopathy. *Circ. Res.* 95:717–725.

23. Tandler, B., L. Riva, …, R. Isola. 2006. High resolution scanning electron microscopy of the intracellular surface of intercalated disks in human heart. *Tissue Cell.* 38:417–420.

24. Hoyt, R. H., M. L. Cohen, and J. E. Saffitz. 1989. Distribution and three-dimensional structure of intercellular junctions in canine myocardium. *Circ. Res.* 64:563–574.

25. Pinali, C., H. Bennett, …, A. Kitmitto. 2013. Three-dimensional reconstruction of cardiac sarcoplasmic reticulum reveals a continuous network linking transverse-tubules: this organization is perturbed in heart failure. *Circ. Res.* 113:1219–1230.

26. Briston, S. J., J. L. Caldwell, …, A. W. Trafford. 2011. Impaired β-adrenergic responsiveness accentuates dysfunctional excitation-contraction coupling in an ovine model of tachypacing-induced heart failure. *J. Physiol.* 589:1367–1382.

27. Dibb, K. M., J. D. Clarke, …, A. W. Trafford. 2009. Characterization of an extensive transverse tubular network in sheep atrial myocytes and its depletion in heart failure. *Circ Heart Fail.* 2:482–489.

28. Schneider, C. A., W. S. Rasband, and K. W. Eliceiri. 2012. NIH Image to ImageJ: 25 years of image analysis. *Nat. Methods.* 9:671–675.

29. Kremer, J. R., D. N. Mastronarde, and J. R. McIntosh. 1996. Computer visualization of three-dimensional image data using IMOD. *J. Struct. Biol.* 116:71–76.

30. Pettersen, E. F., T. D. Goddard, …, T. E. Ferrin. 2004. UCSF Chimera—a visualization system for exploratory research and analysis. *J. Comput. Chem.* 25:1605–1612.

31. Gürtler, A., N. Kunz, …, A. Posch. 2013. Stain-Free technology as a normalization tool in Western blot analysis. *Anal. Biochem.* 433: 105–111.

32. Forbes, M. S., and N. Sperelakis. 1982. Association between mitochondria and gap junctions in mammalian myocardial cells. *Tissue Cell.* 14:25–37.

33. Fry, C. H., R. P. Gray, …, N. S. Peters. 2014. Architectural correlates of myocardial conduction: changes to the topography of cellular coupling, intracellular conductance and action potential propagation with hypertrophy in guinea-pig ventricular myocardium. *Circ. Arrhythm Electrophysiol.* 7:1198–1204.

34. Wilson, A. J., R. Schoenauer, …, P. M. Bennett. 2014. Cardiomyocyte growth and sarcomerogenesis at the intercalated disc. *Cell. Mol. Life Sci.* 71:165–181.

35. Lu, S., D. E. Borst, and R. Horowits. 2005. N-RAP expression during mouse heart development. *Dev. Dyn.* 233:201–212.

36. Zhang, J. Q., B. Elzey, …, R. Horowits. 2001. Ultrastructural and biochemical localization of N-RAP at the interface between myofibrils and intercalated disks in the mouse heart. *Biochemistry.* 40:14898–14906.

37. Dirkx, E., P. A. da Costa Martins, and L. J. De Windt. 2013. Regulation of fetal gene expression in heart failure. *Biochim. Biophys. Acta.* 1832:2414–2424.

38. Agnetti, G., V. L. Halperin, …, J. E. Van Eyk. 2014. Desmin modifications associate with amyloid-like oligomers deposition in heart failure. *Cardiovasc. Res.* 102:24–34.

39. Rappaport, L., and J. L. Samuel. 1988. Microtubules in cardiac myocytes. *Int. Rev. Cytol.* 113:101–143.

40. Wang, X., F. Li, …, A. M. Gerdes. 1999. Chronic pressure overload cardiac hypertrophy and failure in guinea pigs: II. Cytoskeletal remodeling. *J. Mol. Cell. Cardiol.* 31:319–331.

41. Schaper, J., R. Froede, …, N. Bleese. 1991. Impairment of the myocardial ultrastructure and changes of the cytoskeleton in dilated cardiomyopathy. *Circulation.* 83:504–514.

42. Severs, N. J., K. S. Shovel, …, C. R. Green. 1989. Fate of gap junctions in isolated adult mammalian cardiomyocytes. *Circ. Res.* 65:22–42.

43. Emdad, L., M. Uzzaman, …, Y. Murata. 2001. Gap junction remodeling in hypertrophied left ventricles of aortic-banded rats: prevention by angiotensin II type 1 receptor blockade. *J. Mol. Cell. Cardiol.* 33:219–231.

44. Matsushita, T., M. Oyamada, …, T. Takamatsu. 1999. Remodeling of cell-cell and cell-extracellular matrix interactions at the border zone of rat myocardial infarcts. *Circ. Res.* 85:1046–1055.

45. Gutstein, D. E., F.-Y. Liu, …, G. I. Fishman. 2003. The organization of adherens junctions and desmosomes at the cardiac intercalated disc is independent of gap junctions. *J. Cell Sci.* 116:875–885.

46. Eckardt, D., M. Theis, …, K. Willecke. 2004. Functional role of connexin43 gap junction channels in adult mouse heart assessed by inducible gene deletion. *J. Mol. Cell. Cardiol.* 36:101–110.

47. Zhuang, J., K. A. Yamada, …, A. G. Kléber. 2000. Pulsatile stretch remodels cell-to-cell communication in cultured myocytes. *Circ. Res.* 87:316–322.